Annals of Biomedical Engineering
https://doi.org/10.1007/s10439-024-03606-w

BMES BIOMEDICAL ENGINEERING SOCIETY

ORIGINAL ARTICLE

Super-Resolving and Denoising 4D flow MRI of Neurofluids Using Physics-Guided Neural Networks

Neal M. Patel[1] · Emily R. Bartusiak[2] · Sean M. Rothenberger[1] · A. J. Schwichtenberg[3] · Edward J. Delp[1,2,4] · Vitaliy L. Rayz[1,5] · on behalf of the Alzheimer's Disease Neuroimaging Initiative

Received: 13 February 2024 / Accepted: 18 August 2024

Abstract

Purpose To obtain high-resolution velocity fields of cerebrospinal fluid (CSF) and cerebral blood flow by applying a physics-guided neural network (div-mDCSRN-Flow) to 4D flow MRI.

Methods The div-mDCSRN-Flow network was developed to improve spatial resolution and denoise 4D flow MRI. The network was trained with patches of paired high-resolution and low-resolution synthetic 4D flow MRI data derived from computational fluid dynamic simulations of CSF flow within the cerebral ventricles of five healthy cases and five Alzheimer's disease cases. The loss function combined mean squared error with a binary cross-entropy term for segmentation and a divergence-based regularization term for the conservation of mass. Performance was assessed using synthetic 4D flow MRI in one healthy and one Alzheimer' disease cases, an in vitro study of healthy cerebral ventricles, and in vivo 4D flow imaging of CSF as well as flow in arterial and venous blood vessels. Comparison was performed to trilinear interpolation, divergence-free radial basis functions, divergence-free wavelets, 4DFlowNet, and our network without divergence constraints.

Results The proposed network div-mDCSRN-Flow outperformed other methods in reconstructing high-resolution velocity fields from synthetic 4D flow MRI in healthy and AD cases. The div-mDCSRN-Flow network reduced error by 22.5% relative to linear interpolation for in vitro core voxels and by 49.5% in edge voxels.

Conclusion The results demonstrate generalizability of our 4D flow MRI super-resolution and denoising approach due to network training using flow patches and physics-based constraints. The mDCSRN-Flow network can facilitate MRI studies involving CSF flow measurements in cerebral ventricles and association of MRI-based flow metrics with cerebrovascular health.

Keywords 4D flow MRI · CSF · Physics-guided neural networks · Machine learning

Associate Editor Stefan M. Duma oversaw the review of this article.

Collaborators of the of the Alzheimer's Disease Neuroimaging Initiative are listed in "Acknowledgment".

✉ Vitaliy L. Rayz
vrayz@purdue.edu

1 Biomedical Engineering, Purdue University, West Lafayette, IN, USA

2 Electrical and Computer Engineering, Purdue University, West Lafayette, IN, USA

3 Health and Human Sciences, Purdue University, West Lafayette, IN, USA

4 Psychological Sciences, Purdue University, West Lafayette, IN, USA

5 Mechanical Engineering, Purdue University, West Lafayette, IN, USA

Introduction

Cerebrospinal fluid (CSF) is produced by the choroid plexus in the cerebral ventricles and surrounds the spinal cord and brain, acting to cushion impact and maintain intracranial pressure. Within the brain, CSF surrounds penetrating arteries in the periarterial space, where it then extravasates into the interstitial space carrying metabolic wastes to the perivenous space. Disruptions to CSF flow are implicated in hydrocephalus-related diseases (such as idiopathic normal pressure hydrocephalus; iNPH) and neurodegenerative diseases (such as Alzheimer's disease; AD) [1, 2]. Further, patients with iNPH and AD often have more vascular risk factors [3, 4]. Evaluation of both blood flow and CSF flow could enable unique insights into the underlying pathophysiology of these diseases.

Published online: 02 September 2024

Phase-contrast MRI is an MRI technique that enables in vivo measurement of flow. Classically, cardiac-gated phase-contrast MRI (PCMRI) has been used to evaluate blood flow [5]. However, in vivo characterization of CSF using 2D PCMRI techniques in the cerebral aqueduct has shown differences in CSF flow rates in many conditions, including aqueductal stenosis [6], AD [7], and iNPH [7]. Time-resolved 3-directional PCMRI (4D flow MRI) could extend this analysis by evaluating shear stress and flow residence time in the ventricles and its relation to cerebral blood flow. Recently, Yamada et al. showed oscillatory shear stress computed from 4D flow MRI is significantly elevated in patients with iNPH [8, 9]. However, estimating oscillatory shear stress and other near-wall velocity related metrics from 4D flow MRI measurements of CSF can lead to large deviations due to image noise and insufficient resolution influenced by long T1 relaxation rates and low velocities.

Several techniques have been developed for reducing noise and improving spatial resolution of vascular 4D flow MRI, including variational [10–12], transfer domain filtering [13–15], data assimilation [16–19], and deep learning approaches [20–24]. Often these methods combine image denoising methods with physical constraints such as conservation of mass. Radial basis functions, for example, can be used to estimate a denoised divergence-free flow field using iterative least squares [12]. Divergence-free wavelets (DFW) with automated techniques for soft thresholding the divergence-free constraint have been proposed to separate the noisy velocity data into the actual divergence minimized flow field and the surrounding noise [13].

Two classes of deep learning methods have emerged for denoising and super-resolving blood flow: traditional convolutional neural networks (CNNs) [21, 23, 24] and physics-informed neural networks [20, 22]. Traditional convolutional approaches enable the association of local flow features to inform denoising and super-resolution. 4DFlowNet is a recently proposed CNN that was trained using both the mean square error of the velocities and of the velocity gradients along their respective spatial direction [21]. This was designed to leverage the advantages of traditional networks while integrating physical constraints. Once trained, these networks can quickly provide high-resolution denoised estimations but are not strictly constrained by conservation of mass and linear momentum. Physics-informed neural networks (PINNs) iteratively approximate the Navier–Stokes equations for each patient case which can lead to long reconstruction times.

Generative adversarial networks (GANs) [25] and vision transformers [26] have grown in use for image super-resolution but remain limited by computational expense and training stability. Here, we draw on work by Daw et al. [27] and extend on work by Ferdian et al. [21] to propose a physics-guided neural network that combines the advantages of fast reconstruction from traditional convolutional network approaches and conservation of mass regularization from physics-informed neural networks. Our proposed physics-guided neural network aims to improve the spatial resolution and denoise 4D flow MRI, while ensuring that the fields are consistent with the principles of flow physics. Further, we uniquely apply these methods to 4D flow MRI of blood and CSF flow.

Our network is trained on patches of paired high-resolution velocity fields and low-resolution synthetic 4D flow MRI representative of CSF flow in the 3rd and 4th ventricles derived from computational fluid dynamics (CFD). Patches are used to reconstruct smaller and intermediate-scale flow structures that may be conserved across unique geometries, rather than those larger flow structures specific to a given geometry. We assess the network performance quantitatively using a test set of synthetic 4D flow MRI of the 3rd and 4th ventricles in healthy and AD cases as well as a flow phantom of the 3rd and 4th ventricles imaged with 4D flow MRI and compared to high-resolution CFD. We qualitatively examine network performance for an in vivo study of CSF flow within the 3rd ventricle of a healthy individual. We assess generalizability by applying the network to in vivo 4D flow MRI of flow through the carotid bifurcation and the transverse sinus in a healthy individual.

Methods

Generation of Synthetic 4D Flow MRI Dataset

Generating synthetic 4D flow MRI from simulated high-resolution velocity fields enables the creation of a diverse dataset without the need for many paired noise-limited high-resolution and low-resolution 4D flow MRI scans of CSF flow in unique individuals. CFD simulations can provide high-resolution physically consistent flow fields that represent fluid flow in the cerebral ventricles. These simulations can be converted to synthetic 4D flow MRI producing paired ground truth high-resolution data and low-resolution synthetic 4D flow MRI that can be used for network training.

According to a Purdue approved IRB protocol, structural and flow images were acquired on five healthy individuals using the Siemens 3T PRISMA MRI at Purdue University. Structural images acquired with T2 SPACE ($1 \times 1 \times 1$ mm, TR/TE/flip-angle = 700 ms/11 ms/120°, acquisition matrix size = 256/256) and T1 MPRAGE ($1 \times 1 \times 1$ mm, TR/TE/flip-angle = 2300 ms/2.26 ms/8°, acquisition matrix size = 256/256) were segmented to create geometries of the third and fourth ventricles for each patient using the open-source software ITK-Snap [28] as shown in Fig. 1A and B. The Alzheimer's Disease Neuroimaging Initiative (ADNI) was used to obtain T1 images of five AD cases between

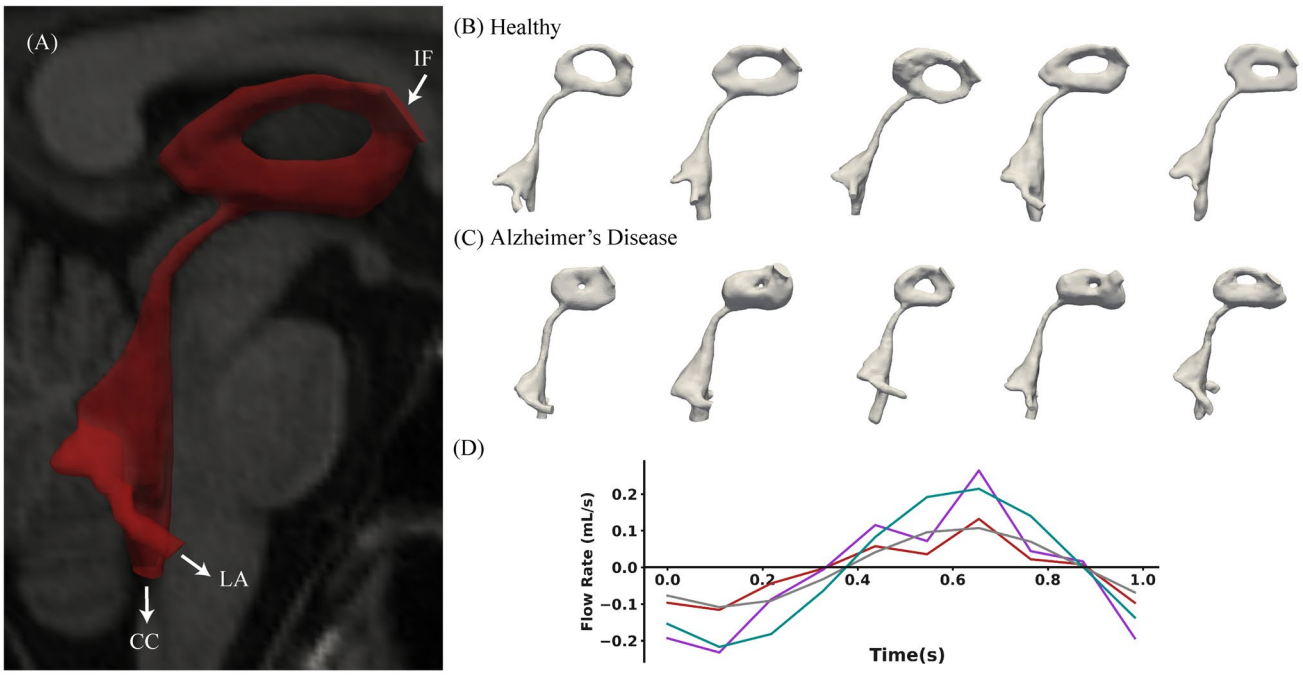

Fig. 1 **A** Structural T1 MPRAGE and T2 SPACE scans were used to segment the 3rd and 4th ventricles. The interventricular foramina (IF) were used as the inlet in CFD simulations, and the central canal (CC) and lateral apertures (LA) were used as the outlets as indicated by the red arrows. One segmented geometry is shown in red. **B** 5 geometries were obtained from healthy individuals and illustrate the diversity of shape present in healthy individuals. **C** 5 additional geometries were obtained from scans of patients with Alzheimer's disease from the ADNI dataset. **D** Unique MR-based inflow waveforms are prescribed for each geometry to generate four simulations per geometry.

59 and 82 years old (acquisition matrix size = 256/256). These images were similarly segmented. The geometries were meshed with surface elements with an average edge size of 0.3 mm. These surface elements were then used to generate volume meshes consisting of tetrahedral elements with an average edge size of approximately 0.4 mm using the commercial software HyperMesh (Altair Engineering Inc., Troy, MI) [29]. This enabled higher mesh density in near wall regions.

A mesh independence was verified in CFD simulations on meshes with average tetrahedral edge sizes of 0.2 mm (3,750,273 elements), 0.4 mm (434,960 elements), and 0.55 mm (234,774 elements). The velocity magnitude and wall shear stress distributions computed on the mesh used in our study showed less than 3% deviation from those computed on the higher density mesh. A comparison of the numerical results obtained on meshes with different densities are shown in Supplemental data. Therefore, an average mesh size of 0.4 mm was deemed sufficient for performing two-fold super-resolution of 4D flow MRI data.

For each geometry, four simulations were performed with varying MR-based inflow conditions at the interventricular foramina to capture a diverse range of flow structures: (1) original 4D flow MRI acquired flow rate in the cerebral aqueduct, (2) its corresponding fit sinusoid, (3) double the acquired flow rate, and (4) its corresponding fit sinusoid, as shown in Fig. 1C. MR-based inflow conditions for AD cases were based on 2D phase-contrast MRI obtained from Daouk et al. [30] The lateral apertures of the 4th ventricle and the central canal were used as zero-pressure outlet boundary conditions indicated by outward-directed arrows in Fig. 1A. No slip conditions were used at the wall. CSF, a fluid with similar properties as water, was modeled as a fluid with a density of 1000.59 kg/m^3 and a viscosity of 0.0011 kg/ms.

Simulations of CSF flow were run in ANSYS Fluent 19.2 from ANSYS Workbench (Ansys, Canonsburg, PA) with a time step of 0.00278 s over two one-second cardiac cycles using a second order implicit transient scheme [31]. The Coupled algorithm was used for pressure-volume coupling. This works by solving the momentum and pressure-based continuity equations simultaneously. Spatial discretization was performed using least squares for gradients, second order for pressures, and third order monotonic upstream-centered scheme for conservation laws (MUSCL) for momentum [32]. Absolute residual criteria of 0.001 were used for continuity of mass and linear momentum. A total of 45 timeframes were saved for each cardiac cycle.

Synthetic 4D flow MRI datasets were generated according to prior work to obtain representative two times spatially downscaled data compared to paired high-resolution data [33, 34]. The process is illustrated in Fig. 2. First, the velocity fields from the 40 simulations performed on the

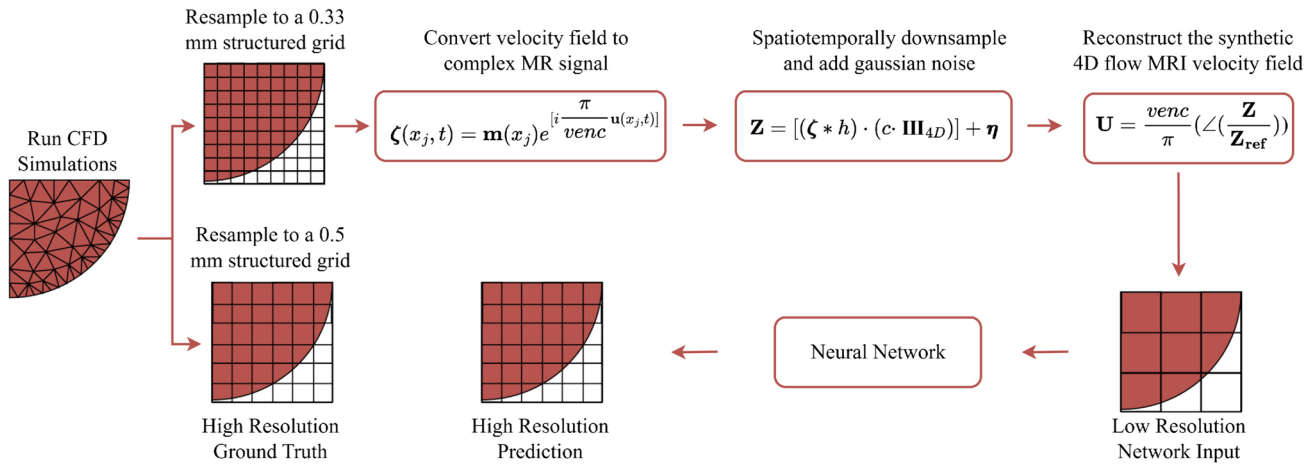

Fig. 2 CFD simulations are run on meshes with unstructured grids. The velocity fields from these simulations are resampled onto two structured grids representative of the voxel grids in MRI. The first resampling is onto a 0.33 mm isotropic structured grid. This signal is converted to a complex MR signal which is spatiotemporally downsampled. Then, gaussian noise is added. The downsampled and noisy MR signal is converted back to a velocity field. This synthetic velocity field and magnitude at a 1 mm isotropic resolution is used as the network input. The second resampling of the unstructured grid onto a 0.5 mm isotropic grid is the high-resolution ground truth used during network training.

geometries from Fig. 1 were interpolated onto two structured grids: one 0.33 × 0.33 × 0.33 mm grid and one 0.5 × 0.5 × 0.5 mm grid. The velocity field on the 0.5 mm isotropic grid is considered the high-resolution ground truth data for network training. Given the kinematic viscosity of CSF along with a heart rate of one beat per second, the estimated thickness of the near-wall layer where viscous effects cause steep velocity gradients was 1.05 mm. This corresponds to two high-resolution 0.5 mm isotropic voxels within this layer [35]. The velocity field ($\boldsymbol{u}$) on the grid with an isotropic voxel size (δ) of 0.33 mm is converted to a complex MR signal (ζ) for all voxels (x_j) over time (t) using a prescribed velocity encoding (*venc*) as follows:

$$\boldsymbol{\zeta}(x_j,t) = \boldsymbol{m}(x_j) \bullet exp\left[i\frac{\pi}{venc}\boldsymbol{u}(x_j,t)\right], \tag{1}$$

where $\boldsymbol{m}$ represents the signal magnitude that depends on the prescribed saturation ratios. The saturation ratio indicates the magnitude of the signal in background voxels relative to the flow voxels. The saturation ratio was set randomly between 0.1 and 0.5 in the training and validation datasets. Similarly, the *venc* to maximum velocity ratio was set randomly between 0.7 and 3 in the training and validation datasets. A *venc* to maximum velocity ratio of less than one will result in phase wrapping of velocities, while higher ratios will be associated with reduced velocity-to-noise ratios. The complex MR signal is downsampled according to (2), by convolving the signal with point spread functions ($\boldsymbol{h}$) and resampling using the Dirac comb function ($\mathbf{III}$) and a coefficient (c) to model the signal proportionality in the downsampled case. The signal is spatially downsampled by a factor of three using a sinc point spread function (PSF) to model sampling and truncation in Cartersian acquired k-space and temporally downsampled by a factor of three using a box PSF to model temporal averaging. Three times spatial downsampling from the 0.33 mm grid was performed using the sinc PSF to model intravoxel dephasing and bias error of 4D flow MRI [33]. Complex gaussian noise (η) between 5 and 50% is added producing images with SNRs ranging between 2 and 20 [33, 36–38].

$$\mathbf{Z} = \left[(\boldsymbol{\zeta} * \mathbf{h}) \cdot \left(c \cdot \mathbf{III}_{4D}\right)\right] + \eta \tag{2}$$

The phase of the signal and a reference signal derived using a zero-vector velocity field is then used to reconstruct the low-resolution noisy synthetic 4D flow MRI ($\boldsymbol{U}$): [39]

$$\mathbf{U} = \frac{venc}{\pi}\left(\angle\frac{\mathbf{Z}}{\mathbf{Z}_{ref}}\right). \tag{3}$$

For each cardiac cycle of each simulation, three unique synthetic cases were generated. The resulting dataset was split using an 8:1:1 ratio for training, validation, and testing reserving unique geometries for validation and testing.

Network Architecture and Training

The network proposed in this work (mDCSRN-Flow), shown in Fig. 3, operates on patches of the segmented, or masked, low-resolution 4D flow MRI data to estimate the corresponding high-resolution masked and denoised velocity field. The network is trained using 9 × 9 × 9 voxel patches from each timestep of the synthetic 4D flow MRI data. By

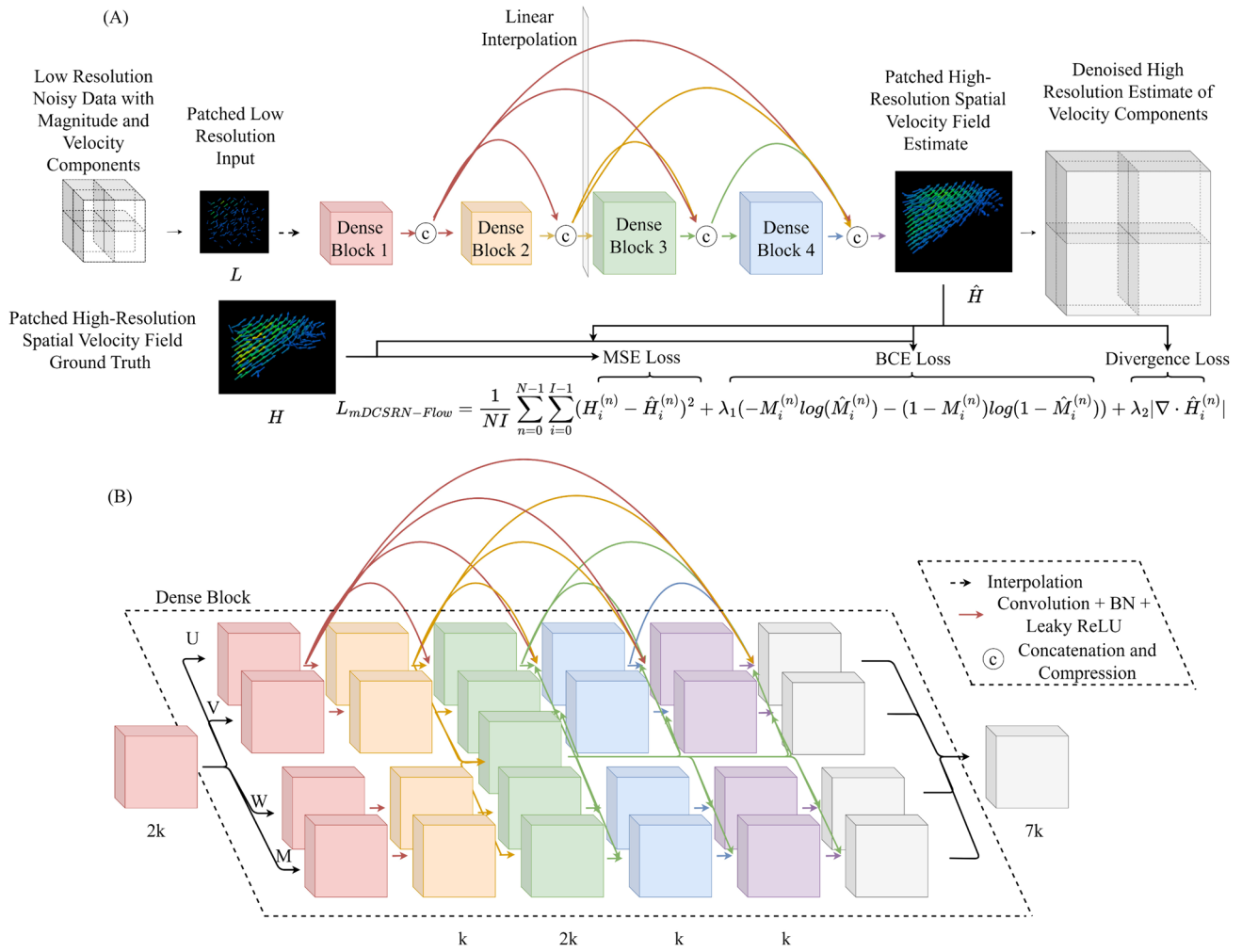

Fig. 3 **A** The network architecture is based on the multi-level densely connected super-resolution network (mDCSRN). The input velocity field and low-resolution masked magnitude pass through two denoising dense layers before the associated features are doubled in scale using trilinear interpolation then passed through the remaining network. The loss function for mDCSRN-Flow relies on mean squared error (MSE) loss with an added binary cross-entropy (BCE) for segmentation. The case with added divergence regularization in the loss term is referred to as div-mDCSRN-Flow. **B** The dense blocks are adapted to accommodate for the higher dimensional data and include cross-stitching as a method for generating velocity and signal magnitude dependent and independent data. Identical skip connections are used for each parallel path but are not illustrated for clarity.

using patches, network training is focused on intermediate and smaller-scale flow structures rather than those dominated by a patient's geometry. The input velocity components are normalized to a range between [−1,1] based on the highest component velocity in the given patch. The signal intensity is normalized to 1 using the maximum intensity in each patch. Patches are randomly rotated and selected for each epoch, with 90% sampled from flow regions and 10% sampled from background regions.

The network architecture is based on a convolutional neural network known as 3D Multi-Level Densely Connected Super-Resolution Network (mDCSRN) architecture [25]; however, several notable modifications were implemented to work on the 3-directional phase-contrast data. To accommodate for the higher dimensionality of 4D flow MRI data, parallel branches are used for super-resolving and denoising the velocity components along the x, y, and z directions and for obtaining a high-resolution mask of the velocity field. These branches are composed of several dense blocks of convolutional layers. Each dense block connects to all succeeding dense blocks [40]. This helps maximize information flow between layers in deep neural networks. The growth rate, k, informs the number of features in a given dense block [25, 40]. Each dense block accepts 2 k input features and produces 7 k output features, with $k = 16$ for the results described in this work. A cross-stitch layer is incorporated in each dense block to balance component independent and dependent features [41]. The cross-stitch

feature set is represented in Fig. 3B by the shared green feature set located between the four channels that is used in the following layers of all branches. Additionally, a linear interpolation layer is added after initial denoising layers, so the overall network spatially upscales the input data by a factor of two. We term this revised network mDCSRN-Flow.

Leaky Rectified Linear Unit (ReLU) was used as the activation function following all illustrated convolution layers. We use the outputs from the different branches of the network to derive a high-resolution mask. The output of the signal intensity path is multiplied by the estimated high-resolution speed. This multiplication of the signal intensity and speed represents the high-resolution phase-contrast magnetic resonance angiogram (PC-MRA). A $1 \times 1 \times 1$ convolution and sigmoid activation function are then applied to the estimated PC-MRA to predict the ultimate mask.

The network was created using PyTorch.[42] Adams optimizer was used with a learning rate of 1e−4. The total network size was 1.98 M parameters. The networks were trained for 100 epochs with 180 iterations of batch size of 32 on NVIDIA A30 graphics processing units.

Loss Functions

The network was trained primarily using a mean squared error (MSE) loss function. We represent the model-predicted high-resolution velocity components as $\widehat{H}$ and the ground truth velocity components as H. The MSE loss can be expressed as

$$\mathcal{L}_{MSE} = \frac{1}{NI} \sum_{n=0}^{N} \sum_{i=0}^{I} \left(H_i^{(n)} - \widehat{H}_i^{(n)} \right)^2, \tag{4}$$

where N represents the number of patches in a given batch, and I represents the number of voxels in a given patch.

The MSE function alone does not ensure physical consistency and is known to smooth results, which could prevent accurate reconstruction of near-wall velocities or regions with steep velocity gradients such as surrounding a jet. We, therefore, assess the benefit of constraining our high-resolution estimations by using a divergence-based regularization term to ensure conservation of mass. Here, we use a cumulative dimensionless divergence loss evaluated over the estimated flow domain ($\mathcal{F}$):

$$\mathcal{L}_{Div} = \frac{1}{NI} \sum_{n=0}^{N} \sum_{i=0}^{I} \left| \nabla \bullet \widehat{H}_i^{(n)} \right| \; if \; i \in \mathcal{F}. \tag{5}$$

This loss term computes a dimensionless divergence by using the patch-normalized velocity field and unit distances assuming the grids are isotropic.

To define those voxels lying within the flow domain, the network is designed to predict a mask for the high-resolution velocity field simultaneously. Mask prediction was constrained by a binary cross-entropy loss term comparing the ground truth mask M with the estimated mask $\widehat{M}$.

$$\mathcal{L}_{Seg} = \frac{1}{NI} \sum_{n=0}^{N} \sum_{i=0}^{I} \left[-M_i^{(n)} log\left(\widehat{M}_i^{(n)} \right) - \left(1 - M_i^{(n)} \right) log\left(1 - \widehat{M}_i^{(n)} \right) \right] \tag{6}$$

The total loss function is the sum of these three terms and can be expressed as

$$\mathcal{L}_{Tot} = \mathcal{L}_{MSE} + \lambda_1 \mathcal{L}_{Seg} + \lambda_2 \mathcal{L}_{Div}, \tag{7}$$

where λ_1 and λ_2 are hyperparameters used to adjust the relative weight of the segmentation and divergence loss terms. In the results described below, λ_1 is set to 0.0016 and λ_2 is set to 0.066. Asynchronous successive halving, implemented with Tune, an open-source python library, was used for the optimization of the following hyperparameters: batch size, patch size, k, λ_1, and λ_2 [43, 44]. The network architecture trained with the complete loss function is termed div-mDCSRN-Flow. As an ablation study, the same network architecture trained without the divergence regularization is termed mDCSRN-Flow. Training and validation curves can be found in Fig. S1.

Synthetic, In Vitro and In Vivo Testing Datasets Using 4D flow MRI Imaging

Once the networks were trained, testing of the network was first performed using synthetic 4D flow MRI data in healthy and AD geometries. Each simulated case included one cardiac cycle of data (15 timeframes) with a MR realistic waveform used. Both synthetic datasets were generated using a saturation ratio of 0.3 [33], 4 *venc* to maximum velocity ratios (0.8, 1.2, 1.6, 2.0), and 4 noise levels (10%, 20%, 30%, 40% noise). Therefore, the healthy and AD test datasets each had datasets including 240 timeframes of paired high-resolution low-resolution velocity fields.

To test the robustness of network performance in reconstruction of denoised high-resolution velocity fields for prospectively gated dual-*venc* 4D flow MRI acquired using the Siemens 3T PRISMA MRI at Purdue University, an in vitro study of flow in the 3rd and 4th ventricles from a healthy participant was conducted [45]. The ventricular geometry was scaled by a factor of 2 in each Cartesian direction to enable imaging of finer flow structures with higher signal-to-noise ratios. The scaled geometry was edited in Geomagic Design software (3D Systems, Rock Hill, SC) to create a luminal surface and to add extensions to connect to a flow loop [46]. The phantom was printed with VisiJet M2R-CL material using a ProJet MJP 2500 Plus printer (3D Systems, Rock Hill, SC). The phantom was connected to the MR-compatible flow loop and a programmable pump circulated water with an inlet flow of 1.2 mL/s directed cranially. More information about the flow loop and a diagram of the setup

is shown in Fig. S2. The two times upscaled in vitro flow phantom was imaged at a $2 \times 2 \times 2$ mm resolution.

This experimental setup was modeled with CFD using ANSYS Fluent according to the protocol described in Section "Generation of Synthetic 4D Flow MRI Dataset". The model contained a single inlet and outlet as illustrated in Fig. S2. Inflow conditions were prescribed at the inlet to match flow meter readings taken during 4D flow acquisition. Zero-pressure outlet boundary conditions were used. These CFD results matched to experimental conditions were projected onto a 1 mm isotropic grid to quantitatively assess performance of the upscaling and denoising neural network when applied to the in vitro 4D flow MRI data.

To assess the generalizability of network performance for various flow conditions and territories, the network was applied to in vivo 4D flow measurements of the CSF flow in the cerebral ventricles and blood flow in the carotid artery bifurcation and transverse sinus acquired using the same Siemens 3T PRISMA MRI with dual-*venc* 4D flow MRI [45]. Dual-*venc* 4D flow MRI was used to improve measurements of slow velocities, while ensuring no phase-wrapping in high velocity regions. For CSF flow imaging, this enables measurements in the cerebral aqueduct that are free of phase wrapping, while maintaining higher velocity-to-noise ratio in the 3rd ventricle by using a lower *venc*. Further, the dual-*venc* sequence allows high quality measurements of both the cerebral arteries and veins. The *vencs* and additional imaging parameters used in the in vitro and in vivo studies are shown in Table 1.

For the in vivo studies presented, a dual-*venc* 4D flow scan of the CSF was taken in a healthy 50-year-old male volunteer and a dual-*venc* 4D flow scan of blood flow was taken in a healthy 25-year-old female volunteer according to the 4D flow MRI protocol approved by Purdue IRB. Once the 4D flow MRI images were acquired, they were input into the network to estimate the high-resolution denoised velocity fields. CSF velocity fields were qualitatively assessed by observing anticipated flow structures and alignment of velocity vectors in the near-wall voxels. The velocity fields within the common carotid bifurcation and transverse sinus were qualitatively assessed by observing alignment of velocities in the near-wall voxels and continuity of streamlines in the vasculature generated using a sphere of 200 points seeded at the vessel inlet in both the obtained 4D flow MRI and in the network high-resolution estimation based on the obtained 4D flow MRI using Paraview [47].

Quantitative Assessment of Synthetic and In Vitro Reconstruction

We assess the accuracy of several methods in doubling the spatial resolution while denoising the velocity fields of synthetic and in vitro 4D flow MRI datasets quantitatively using the cumulative normalized divergence and the root-mean-square error (RMSE) of the normalized velocity components. The RMSE of the velocity components is computed as follows:

$$RMSE = \frac{\sum_{i=1}^{I} \sqrt{[(\hat{u}_i - u_i)^2 + (\hat{v}_i - v_i)^2 + (\hat{w}_i - w_i)^2]}}{I} \tag{8}$$

where $\hat{u}, \hat{v}$, and $\hat{w}$ represent the estimated patch-normalized velocity components in the x, y, and z directions, respectively. u, v, and w represent the known high-resolution patch-normalized velocities, and I represents the total number of voxels assessed. Patch-normalized root-mean-square error promotes higher error weighting of low velocity regions as compared to traditional RMSE of the velocity field alone. Simultaneously, this analysis does not over emphasize the error in low velocity regions as would occur in percent error analysis. We evaluate this metric in both the core flow regions and the edge flow regions as defined by those voxels immediately adjacent to background voxels.

Our analysis focused on the comparison of several techniques for denoising and super-resolving 4D flow MRI measurements. Here, we compare trilinear interpolation (TLI), divergence-free radial basis functions (RBF) [12], divergence-free wavelet (DFW) transforms using SureShrink and cycle-spinning [13], 4DFlowNet [21], our network with ablation of the divergence loss-term (mDCSRN-Flow), and

Table 1 Imaging parameters for 4D flow MRI acquisitions in in vitro studies and an in vivo study

	Ventricular in vitro	Ventricular in vivo	Vascular in vivo
Isotropic voxel size (mm)	2	1.1	1
High *venc* (cm/s)	40	6	70
Low *venc* (cm/s)	20	4	35
TR (ms)	6.4	9.8	6.7
TE (ms)	3.97	7.2	4.01
Flip angle	15	8	15
Number of cardiac phases	10	12	12
Number of slices	72	64	80
Reconstructed matrix size	192×48	160×80	160×110

our network with divergence regularization (div-mDCSRN-Flow). Code provided by Ong et al. was used for RBFs and DFWs [13]. 4DFlowNet was reimplemented in Pytorch [42]. The total network size was 3.4 M parameters. 4DFlowNet was trained for 100 epochs using the same dataset as in mDCSRN-Flow and div-mDCSRN-Flow. Training and validation curves are shown in Fig. S1 The patch size was adjusted to nine to remain conserved with mDCSRN-Flow and div-mDCSRN-Flow.

Results

Synthetic 4D flow MRI Reconstruction in Healthy Ventricles

We qualitatively examine the performance of TLI, RBF, DFW, mDCSRN-Flow, and div-mDCSRN-Flow on the reconstruction of high-resolution data given synthetic

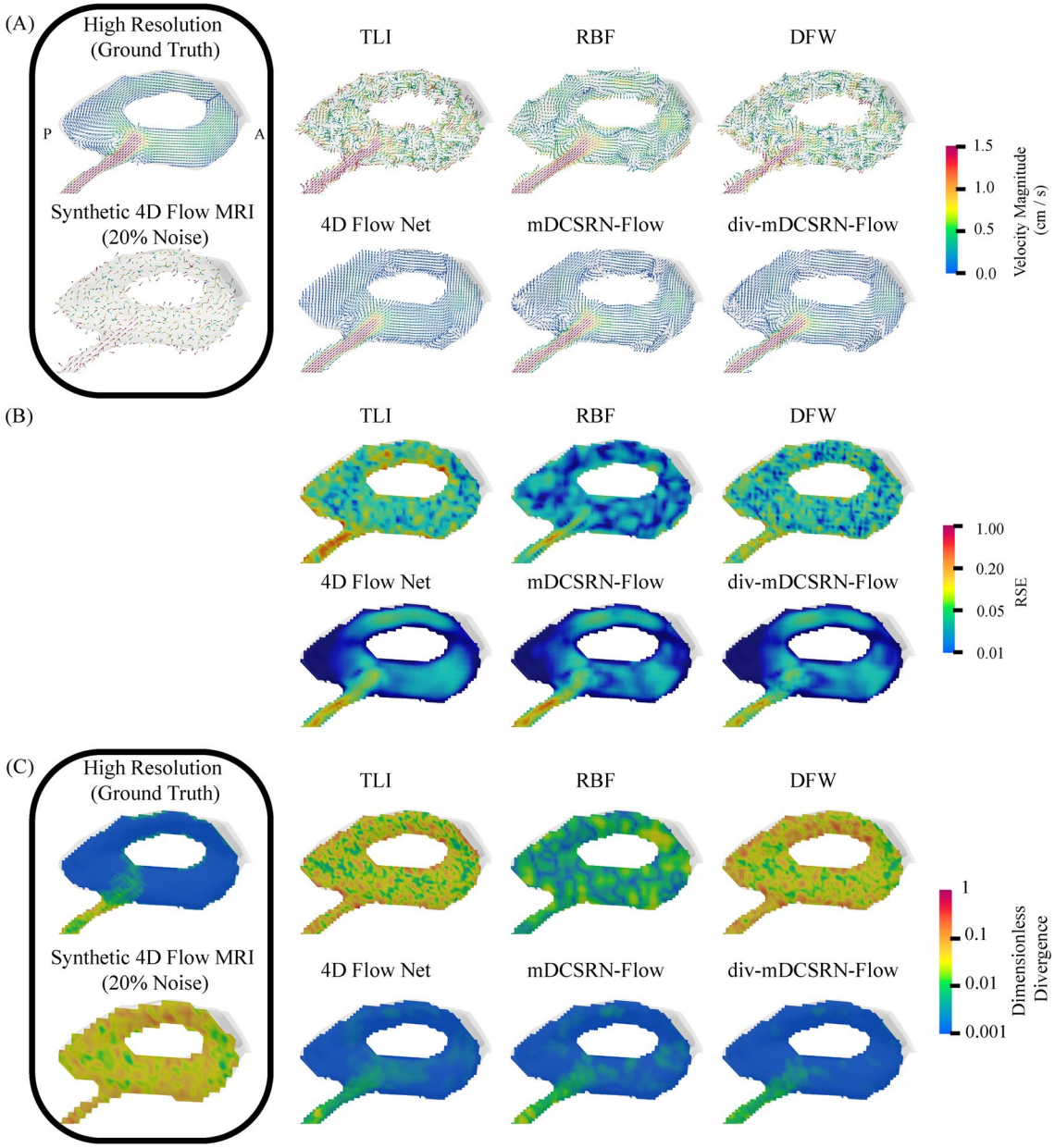

Fig. 4 Synthetic 4D flow MRI generated from CFD within healthy 3rd and 4th ventricles with 20% noise is reconstructed using trilinear linear interpolation (TLI), divergence-free radial basis functions (RBF), divergence-free wavelets (DFW), 4DFlowNet, mDCSRN-Flow, and div-mDCSRN-Flow. Shown is **A** a slice of the flow in the 3rd ventricle with labeled anterior, A, and posterior, P, directions; **B** the root-square error (RSE) of the velocity components; **C** dimensionless divergence.

4D flow MRI data with 20% noise. From Fig. 4A, we see that all methods reasonably reconstruct the dominant flow structure of the cranially directed jet in the 3rd ventricle. This jet is defined by geometry and high velocity, so it is expected to be resolved by 4D flow MRI. By examining the error maps in Fig. 4B, we see that all methods reasonably reconstruct the jet flow; however, the performance of neural network methods, including mDCSRN-Flow, div-mDCSRN-Flow, and 4DFlowNet, shows a relatively greater improvement in slow flow regions within the ventricles, particularly in the posterior aspect of the 3rd ventricle. The log-scaled patch-normalized root-square error (RSE) maps in Fig. 4B and the log-scaled patch-normalized dimensionless divergence maps are shown in Fig. 4C.

We quantitatively assess the reconstruction using the six methods over the 240 timeframes using the RMSE metric for core voxels and edge voxels as defined in section "Quantitative Assessment of Synthetic and In Vitro Reconstruction". Table 2 shows an 83.0% reduction in the RMSE of core voxels and a 95.5% reduction in RMSE of edge voxels using mDCSRN-Flow as compared to trilinear interpolation. The div-mDCSRN-Flow network resulted in the best performance with an 83.6% reduction in core voxels and 96.3% reduction in edge voxels compared to trilinear interpolation. The distribution of core and edge RMSE across all methods in the 240 simulated cases is shown by violin plots in Fig. 7A and B. Lastly, we show the cumulative dimensionless divergence in mDCSRN-Flow and div-mDCSRN-Flow results was 8.1e−4 and 4.2e−4, respectively.

3.2 Synthetic 4D flow MRI Reconstruction in Alzheimer's Disease Ventricles

Network assessment was next performed using synthetic 4D flow MRI in a case of Alzheimer's disease. We again qualitatively assess performance using the case of synthetic data with 20% noise as shown in Fig. 5. The velocity fields are shown in Fig. 5A. Figure 5B and C show maps of the RSE and the dimensionless divergence fields, respectively.

Quantitative assessment of the 240 frames of paired data for both RMSE and dimensionless divergence is presented in Fig. 7D–F. From Table 2, we see mDCSRN-Flow results

Table 2 The root-mean-square error (RMSE) and cumulative dimensionless divergence of high-resolution reconstruction of CFD derived synthetic 4D flow MRI in the healthy and AD cerebral ventricles, and in vitro 4D flow MRI in a 3D printed phantom of the cerebral ventricles using trilinear interpolation (TLI), divergence-free radial basis functions (RBF), divergence-free wavelets (DFW), 4DFlowNet, mDCSRN-Flow, and div-mDCSRN-Flow with the best performance bolded

Synthetic healthy ventricle	Core RMSE		Edge RMSE		Cumulative dimensionless divergence ($\times 10^3$)	
	Mean	Std	Mean	Std	Mean	Std
TLI	0.127	0.0497	0.254	0.0497	33.0	12.4
RBF	0.072	0.0274	0.048	0.0274	4.89	1.90
DFW	0.124	0.0493	0.251	0.0876	32.2	12.4
4DFlowNet	0.021	0.0736	0.010	0.0044	0.62	0.09
mDCSRN-flow	0.021	0.0709	0.011	0.0042	0.81	0.16
div-mDCSRN-flow	**0.020**	0.0726	**0.009**	0.0039	**0.42**	0.16
Synthetic AD ventricle	Mean	Std	Mean	Std	Mean	Std
TLI	0.119	0.0440	0.242	0.0835	73.8	27.2
RBF	0.063	0.0229	0.060	0.2272	10.8	4.12
DFW	0.115	0.0431	0.238	0.0825	71.3	26.5
4DFlowNet	0.023	0.0075	0.011	0.0045	1.28	0.39
mDCSRN-flow	0.022	0.0064	0.012	0.0041	1.95	0.58
div-mDCSRN-flow	**0.021**	0.0065	**0.011**	0.0040	**1.18**	0.57
In vitro ventricle reconstruction	Core RMSE		Edge RMSE		Cumulative dimensionless divergence ($\times 10^3$)	
TLI	0.0632		0.095		21.3	
RBF	0.0644		0.080		9.63	
DFW	0.0630		0.095		21.0	
4DFlowNet	0.0552		0.069		6.34	
mDCSRN-flow	0.0581		0.052		2.40	
div-mDCSRN-flow	**0.0490**		**0.048**		**1.26**	

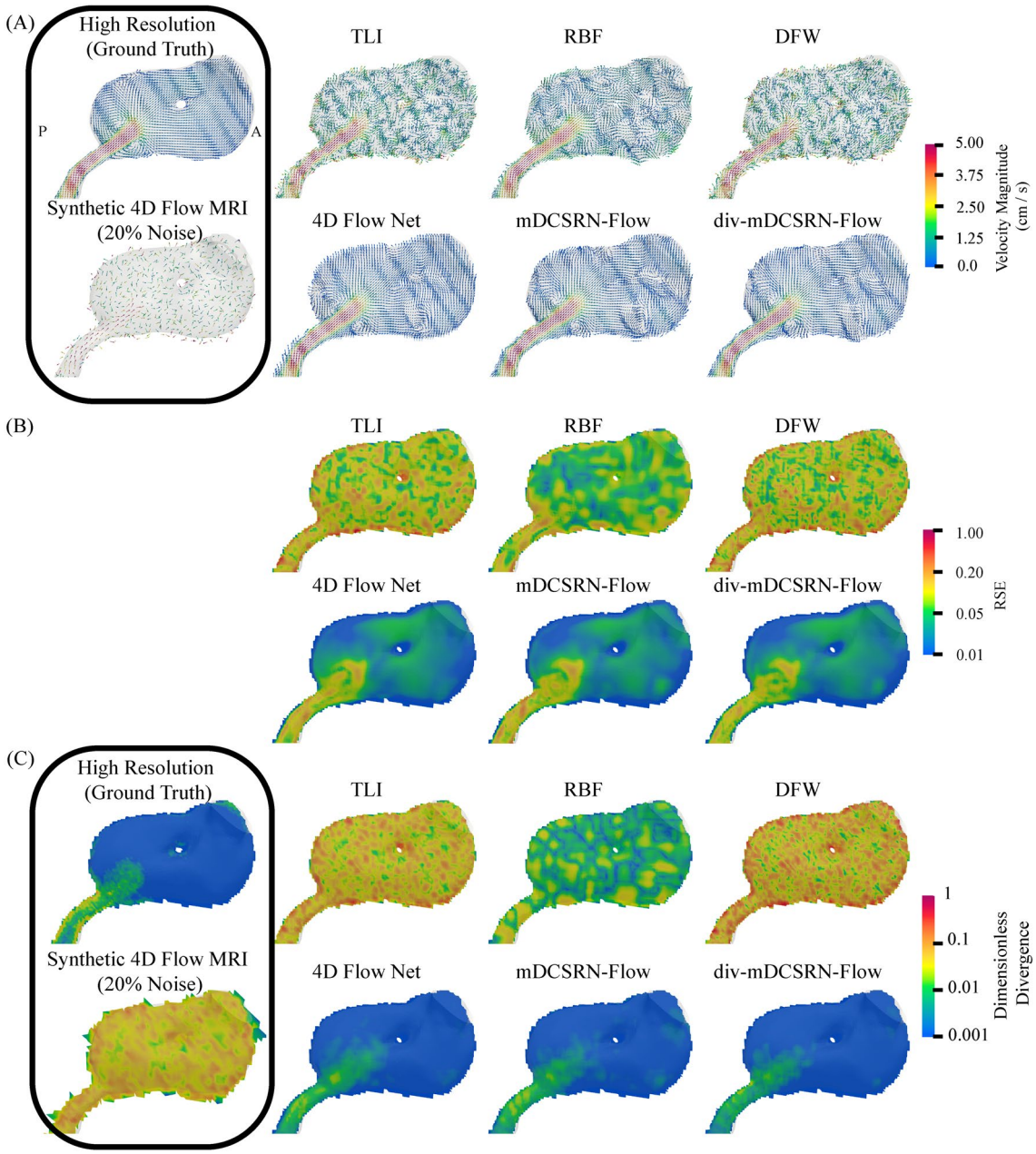

Fig. 5 Synthetic 4D flow MRI generated from CFD in an Alzheimer's Disease (AD) with 20% noise is reconstructed using trilinear linear interpolation (TLI), divergence-free radial basis function (RBF), divergence-free wavelets (DFW), 4DFlowNet, mDCSRN-Flow, and div-mDCSRN-Flow. Shown is **A** a slice of the velocity field; **B** the root-square error (RSE) of the velocity components; and **C** the dimensionless divergence.

in an 81.5% reduction in core RMSE and a 94.8% reduction in edge RMSE relative to linear interpolation. Using div-mDCSRN-Flow results in an 81.7% reduction in core RMSE and a 95.4% reduction in edge RMSE.

In Vitro Validation Using Scaled 3D-Printed Phantom

Using a two-times scaled 3D-printed healthy ventricle phantom, we can image flow in the 3rd ventricle and perform CFD matched to the experimental conditions. The $2 \times 2 \times 2$ mm resolution 4D flow acquisition is used as the network input and reconstructed using TLI, RBF, DFW, 4DFlowNet, mDCSRN-Flow, and div-mDCSRN-Flow. The reconstructions are qualitatively compared to the paired CFD simulation. Slices of the 3rd ventricle, shown in Fig. 6A, reveal similar jet reconstruction compared to the CFD simulation. However, there are noticeable differences in the reconstruction of the slow flowing CSF along the posterior portion of

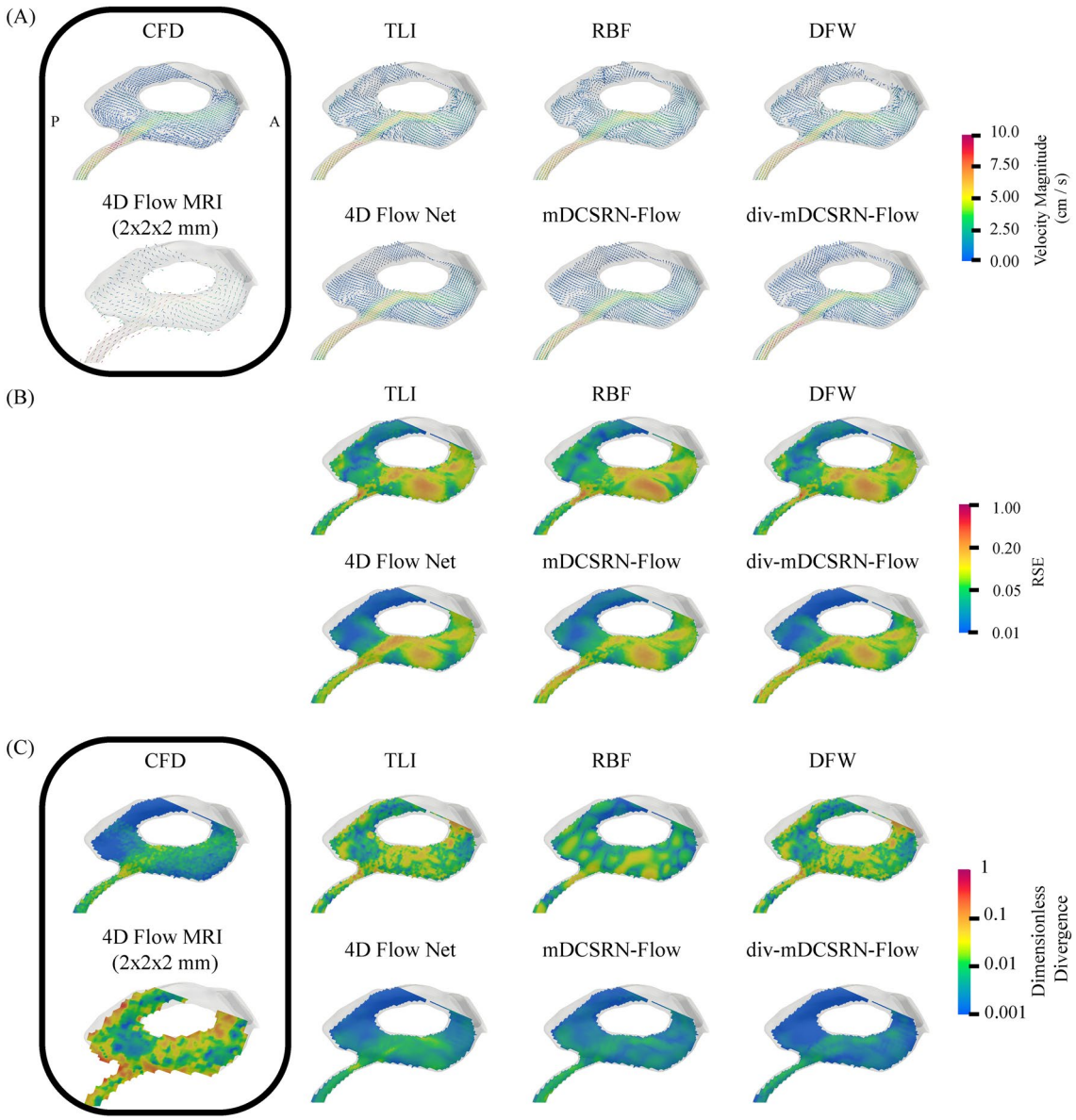

Fig. 6 Reconstruction of in vitro 4D flow MRI acquired in 3D printed phantom compared to high-resolution CFD. **A** Cross-section of velocity field in the 3rd ventricle shows a cranially directed jet with surrounding counter-rotating vortices. **B** The RSE maps and **C** the cumulative dimensionless divergence are shown for TLI, RBF, DFW, 4DFlowNet, mDCSRN-Flow, and div-mDCSRN-Flow.

the 3rd ventricle and among near-wall velocities. The RSE maps are shown in Fig. 6B, and the divergence maps are shown in Fig. 6C.

The div-mDCSRN-Flow again performs best in reduction of the error in core voxels, edge voxels and cumulative dimensionless divergence as shown in Fig. 7H and Table 2.

In Vivo Applications

We apply the div-mDCSRN-Flow network to reconstruct healthy subjects' 4D flow MRI of flow in the cerebral ventricles, carotid artery bifurcation, and transverse sinus. The scans were acquired at a $1 \times 1 \times 1$ mm resolution and super-resolved to $0.5 \times 0.5 \times 0.5$ mm resolution. Shown in Fig. 8A is a slice of the flow field in the 3rd ventricle during systole and diastole. As expected, we see caudally directed flow during systole and cranially directed flow during diastole. Network reconstruction of the velocity field illustrates underlying jets and vortices within the 3rd ventricle similar to CFD simulations in healthy ventricles shown in Fig. 4. Further, we see greater alignment of near-wall velocities with the wall as compared to the raw data. However, there is noticeable smoothing of the jets. Additionally, we see a high-velocity region within the superior portion of the third

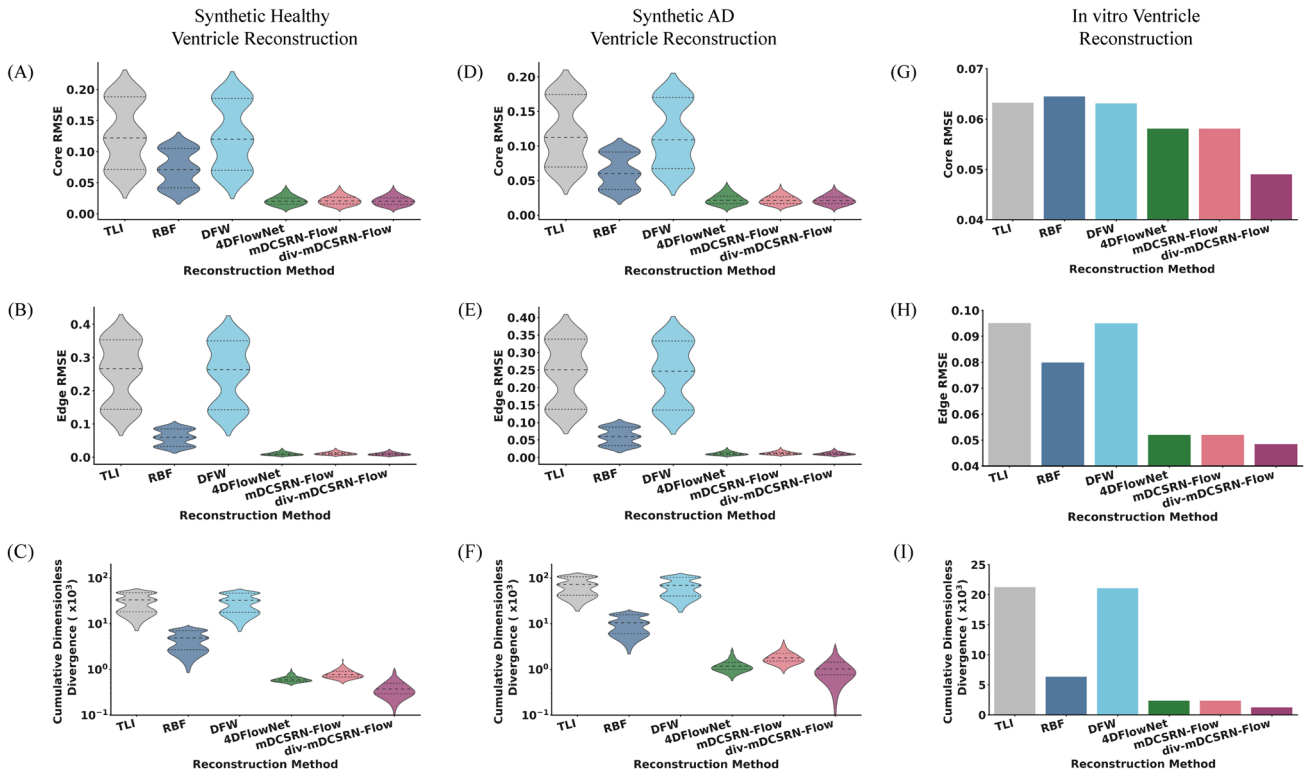

Fig. 7 The reconstruction performance of trilinear interpolation (TLI; grey), divergence-free radial basis functions (RBF; dark blue), divergence-free wavelets (DWW; light blue), 4DFlowNet (green), mDCSRN-Flow (pink), div-mDCSRN-Flow (purple) for three test cases: synthetic 4D flow MRI in healthy ventricles **A**–**C**, synthetic 4D flow MRI in AD ventricles **D**–**F**, and an in vitro dataset of 4D flow MRI acquired in a ventricular phantom **G**–**I**. In vitro performance was compared to high-resolution CFD. Performance is assessed quantitatively using the RMSE in core voxels (row 1) and edge voxels (row 2), as well as the cumulative dimensionless divergence (row 3).

ventricle attributed to the internal cerebral vein lying within the third ventricle. Fig. 8B and C highlight the generalizability of these techniques to vascular flow cases. In both the carotid artery bifurcation and the transverse sinus, we see greater length and retention of streamlines within the vasculature. In Fig. S4, we see application of div-mDCSRN-Flow to the flow measured in the 4th ventricle.

Discussion

In this work, we have developed div-mDCSRN-Flow, a divergence-regularized neural network, to increase resolution and denoise 4D flow MRI measurements of neurofluid flow. While CFD simulations can provide high resolution velocity fields in subject-specific geometries, numerical results can be affected by the uncertainty in the boundary conditions. Prescribing subject-specific boundary conditions is particularly challenging for modeling CSF flow in the ventricles [48]. 4D flow MRI enables in vivo measurements; however, the accuracy is limited due to imaging resolution and noise. The bias error of 4D flow MRI in partial volume voxels may be increased by an order of magnitude [33]. Here we leverage CFD results obtained for a range of physiologically reasonable boundary conditions to generate paired synthetic 4D flow MRI data for training our denoising and super-resolving network.

We assessed the performance of the mDCSRN-Flow network trained without divergence-regularization (mDCSRN-Flow) and with divergence-regularization (div-mDCSRN-Flow). By incorporating both a binary cross-entropy loss term and a cumulative dimensionless divergence regularization term into our physics-guided network, we encouraged the network to both identify the flow domain and produce high-resolution velocity field estimations that abide by conservation of mass. By using the velocity fields as the network input and training using synthetic 4D flow MRI with a diverse range of noise conditions, these networks are expected to be agnostic to 4D flow MRI variability across different imaging sequences and MRI scanners. We quantitatively compared these networks to various reconstruction methods including trilinear interpolation, divergence-free RBFs, DFWs, and 4DFlowNet in synthetic and in vitro studies. Further, we qualitatively tested the proposed network performance in synthetic, in vitro, and in vivo cases.

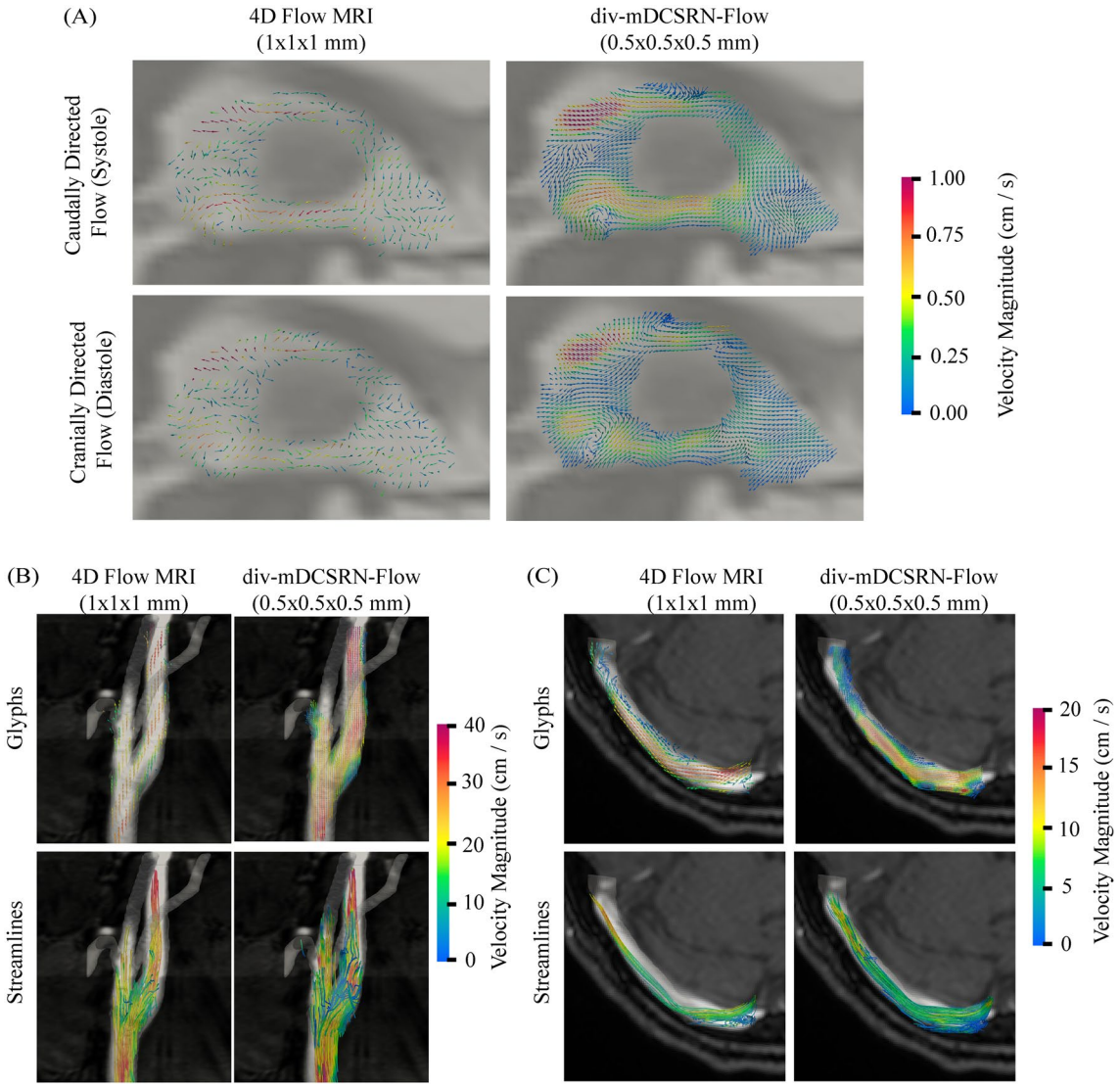

Fig. 8 In vivo 4D flow MRI and div-mDCSRN-Flow reconstructions of CSF and blood flow. **A** Reconstruction in the 3rd ventricle shows caudally directed flow during systole and cranially directed flow during diastole. For blood flow images, div-mDCSRN-Flow shows alignment of near-wall voxels and greater streamline length in high-resolution estimation of flow in the carotid artery bifurcation **B** and in the transverse sinus **C**.

The results showed that div-mDCSRN-Flow and 4DFlowNet similarly outperformed other methods in reconstructing high-resolution velocity fields from synthetic 4D flow MRI in the 3rd and 4th ventricles of healthy and AD individuals in both core voxels and edge voxels. We showed that for both healthy and AD cases, div-mDCSRN-Flow enabled reduction in RMSE in core voxels by greater than 80% and in edge voxels by greater than 95% compared to trilinear interpolation. While the dominant flow patterns in the network reconstructions often look similar to the trilinear interpolation reconstructions, the reduction in normalized divergence indicates that the velocity fields are fine-tuned to be physically consistent. Further, here we see that convolutional neural network-based approaches appeared to outperform non-network-based approaches. This could be because the receptive field enables use of the dominant flow structures to inform denoising within a given patch rather than considering local neighborhoods.

While the in vitro flow study using a 3D-printed ventricular phantom presented does not incorporate effects of background tissue and the complex gating of CSF, it enables controlled 4D flow acquisition which can be used to run CFD matched to experimental conditions that can be used for quantitative assessment. The div-mDCSRN-Flow network reduces error in the in vitro case by 22.5% relative to trilinear interpolation in core voxels and by 49.5% in edge voxels. These results suggest that the network enables the use of the core flow regions to better inform the

reconstruction of near-wall velocities. This is also indicated by the lower cumulative dimensionless divergence relative to interpolation in near-wall voxels. The specific use of a physics-guided loss function ensures mass conservation of the estimated flow fields. Further, divergence-regularization improves network performance in in vitro reconstruction.

While no ground truth data exists for quantitative evaluation of in vivo performance, applying the trained network to an in vivo scan of the 4th ventricle showed improved alignment of near-wall velocity vectors with the wall in partial volume voxels compared to the unprocessed velocity field. Further, we see CSF flow patterns within the third ventricle during systole and diastole are consistent with flow descriptions originally presented by Stadlbauer et al. [49].

However, there appears to be some smoothing of the core flow through the 3rd ventricle during systole and diastole. Further, we see misaligned flow in near-wall voxels where surrounding core tissue has low velocity-to-noise ratios as shown in the anterior aspect of the 3rd ventricle in Fig. 8A. In Fig. S4, we show CSF flow reconstructions within the 4th ventricle highlighting oscillatory flow patterns are consistent with descriptions by Stadlbauer et al. [49].

To demonstrate generalizability of our approach to 4D flow measurements of cerebrovascular flow, our network was applied to arterial flow through the carotid artery bifurcation and to venous flow through the transverse sinus. Despite the network being trained on CSF flow through the ventricles, we observed an improved alignment of near-wall velocity vectors in partial volume voxels with the flow direction in the core flow voxels. We believe that this approach can facilitate studies where 4D flow MRI is used to assess the relationship between cerebral blood flow and CSF flow by denoising and super-resolving both sets of measurements [50, 51]. Translating these methods to super-resolution of 4D flow MRI in transitional flow through larger blood vessels would require a training dataset with higher spatial and temporal resolutions to capture underlying flow features. Herein, our training dataset simulations are focused on CSF flow through the larger ventricles with a maximum Reynolds number of 550, thus sufficient for upscaling and denoising laminar flow measurements.

This study has several limitations. First, ventricular geometries were obtained from healthy volunteers and AD cases. While successful flow reconstruction in AD cases suggest network generalizability to pathologic conditions, there are diverse cerebroventricular diseases with unique anatomical features. We believe the use of patches and physical constraints enables generalizability of the network as indicated by the application to 4D flow MRI in arterial and venous flow. Second, the generation of synthetic 4D flow MR data does not account for eddy current effects, displacement artifacts [52] or the complex movements of the cerebral ventricles. In particular, the generation of synthetic cardiac-gated data does not account for MRI measurement error due to flow-related changes from respiratory gating or low-frequency oscillations [53]. Third, the relatively coarse resolution of 0.5 mm isotropic voxels used to obtain ground truth images leads to increased divergence, especially in regions of rapidly changing velocities (e.g. jet regions). Additionally, the presented methodology focuses on single-frame super-resolution and does not consider temporal information when estimating high-resolution velocity fields [54–57].

Wall shear stress and associated hemodynamic metrics have been associated with cerebrovascular and cerebroventricular disease [58–60]. While CFD can provide high-resolution velocity fields for computing these metrics, CFD results may be limited by the assumptions in image segmentation and boundary conditions. 4D flow MRI enables computation of WSS from in vivo data but affected by image noise and limited spatial resolution, particularly within the boundary layer. 4D flow measurements of CSF flow at a 1 mm isotropic resolution may provide only one data point within the boundary layer, as can be estimated using the Womersley number calculated with a heart rate of 1 beat per second and a kinematic viscosity of $1.099\frac{mm^2}{s}$ [35]. Performing two-times upscaling and denoising using div-mDCSRN-Flow, which doubles the points within the boundary layer, could enable better estimation of WSS from 4D flow data. Improved imaging resolution or higher upscaling could further improve WSS estimation but remains limited by low signal-to-noise ratio and increased computational cost.

This study demonstrated that using a divergence-regularized loss function can produce velocity fields that not only enable better estimation of near-wall velocities, but also ensure those estimations abide by conservation of mass. This methodology could aid studies of CSF flow within the cerebral ventricles in characterizing the effects of near-wall velocity-related metrics to study diseases, such as iNPH or AD, as well as their relation to cerebrovascular health.

Supplementary Information The online version contains supplementary material available at https://doi.org/10.1007/s10439-024-03606-w.

Acknowledgements The authors would like to acknowledge Dr. Michael Markl for his help with sequence optimization and testing, Dr. Xiaopeng Zhou for her help in in vitro and in vivo imaging, and Moses Hamm for his help in dataset generation. This work was partially funded by the NIH awards R01 HL115267 and S10 OD0122336 as well as by the Purdue Institute of Integrative Neuroscience (PIIN) Grand Challenges Award. Data collection and sharing for this project was partially funded by the Alzheimer's Disease Neuroimaging Initiative (ADNI) (National Institutes of Health Grant U01 AG024904) and DOD ADNI (Department of Defense award number W81XWH-12-2-0012). ADNI is funded by the National Institute on Aging, the National Institute of Biomedical Imaging and Bioengineering, and through generous contributions from the following: AbbVie, Alzheimer's Association; Alzheimer's Drug Discovery Foundation; Araclon Biotech; BioClinica, Inc.; Biogen; Bristol-Myers Squibb Company; CereSpir, Inc.; Cogstate; Eisai Inc.; Elan Pharmaceuticals, Inc.; Eli Lilly and Company; EuroImmun; F. Hoffmann-La Roche Ltd and its affiliated company

Genentech, Inc.; Fujirebio; GE Healthcare; IXICO Ltd.; Janssen Alzheimer Immunotherapy Research & Development, LLC.; Johnson & Johnson Pharmaceutical Research & Development LLC.; Lumosity; Lundbeck; Merck & Co., Inc.; Meso Scale Diagnostics, LLC.; NeuroRx Research; Neurotrack Technologies; Novartis Pharmaceuticals Corporation; Pfizer Inc.; Piramal Imaging; Servier; Takeda Pharmaceutical Company; and Transition Therapeutics. The Canadian Institutes of Health Research is providing funds to support ADNI clinical sites in Canada. Private sector contributions are facilitated by the Foundation for the National Institutes of Health (www.fnih.org). The grantee organization is the Northern California Institute for Research and Education, and the study is coordinated by the Alzheimer's Therapeutic Research Institute at the University of Southern California. ADNI data are disseminated by the Laboratory for Neuro Imaging at the University of Southern California. Data used in preparation of this article were obtained from the Alzheimer's Disease Neuroimaging Initiative (ADNI) database (adni.loni.usc.edu). As such, the investigators within the ADNI contributed to the design and implementation of ADNI and/or provided data but did not participate in analysis or writing of this report. A complete listing of ADNI investigators can be found at: http://adni.loni.usc.edu/wp-content/uploads/how_to_apply/ADNI_Acknowledgement_List.pdf

Declarations

Conflict of interest The authors have no relevant financial or non-financial interests to disclose.

References

1. Kylkilahti, T. M., et al. Achieving brain clearance and preventing neurodegenerative diseases: A glymphatic perspective. *Journal of Cerebral Blood Flow & Metabolism*. 41(9):2137–2149, 2021. https://doi.org/10.1177/0271678x20982388.
2. Bramall, A. N., E. S. Anton, K. T. Kahle, and P. E. Fecci. Navigating the ventricles: Novel insights into the pathogenesis of hydrocephalus. *eBioMedicine*. 78:103931, 2022. https://doi.org/10.1016/j.ebiom.2022.103931.
3. Israelsson, H., et al. Vascular risk factors in INPH. *Neurology*. 88(6):577–585, 2017. https://doi.org/10.1212/wnl.0000000000003583.
4. O'Brien, J. T., and H. S. Markus. Vascular risk factors and Alzheimer's disease. *BMC Medicine*. 12:1, 2014. https://doi.org/10.1186/s12916-014-0218-y.
5. Soulat, G., P. McCarthy, and M. Markl. 4D Flow with MRI. *Annu Rev Biomed Eng*. 22:103–126, 2020. https://doi.org/10.1146/annurev-bioeng-100219-110055.
6. Stoquart-El-Sankari, S., et al. Phase-Contrast MR Imaging Support for the Diagnosis of Aqueductal Stenosis. *American Journal of Neuroradiology*. 30(1):209–214, 2009. https://doi.org/10.3174/ajnr.a1308.
7. El Sankari, S., et al. Cerebrospinal fluid and blood flow in mild cognitive impairment and Alzheimer's disease: a differential diagnosis from idiopathic normal pressure hydrocephalus. *Fluids and Barriers of the CNS*. 8(1):12, 2011. https://doi.org/10.1186/2045-8118-8-12.
8. Yamada, S., et al. Cerebrospinal fluid dynamics in idiopathic normal pressure hydrocephalus on four-dimensional flow imaging. *Eur Radiol*. 30(8):4454–4465, 2020. https://doi.org/10.1007/s00330-020-06825-6.
9. Yamada, S., et al. Quantification of Oscillatory Shear Stress from Reciprocating CSF Motion on 4D Flow Imaging. *AJNR Am J Neuroradiol*. 42(3):479–486, 2021. https://doi.org/10.3174/ajnr.A6941.
10. P. D. Tafti, R. Delgado-Gonzalo, A. F. Stalder, and M. Unser, "Variational enhancement and denoising of flow field images," in *2011 IEEE International Symposium on Biomedical Imaging: From Nano to Macro*, 30 March-2 April 2011 2011, pp. 1061-1064, https://doi.org/10.1109/ISBI.2011.5872584.
11. E. Bostan, O. Vardoulis, D. Piccini, P. D. Tafti, N. Stergiopulos, and M. Unser, "Spatio-temporal regularization of flow-fields," in *2013 IEEE 10th International Symposium on Biomedical Imaging*, 7-11 April 2013 2013, pp. 836-839, https://doi.org/10.1109/ISBI.2013.6556605.
12. Busch, J., D. Giese, L. Wissmann, and S. Kozerke. Reconstruction of divergence-free velocity fields from cine 3D phase-contrast flow measurements. *Magn Reson Med*. 69(1):200–210, 2013. https://doi.org/10.1002/mrm.24221.
13. Ong, F., et al. Robust 4D flow denoising using divergence-free wavelet transform. *Magn Reson Med*. 73(2):828–842, 2015. https://doi.org/10.1002/mrm.25176.
14. Bakhshinejad, A., A. Baghaie, A. Vali, D. Saloner, V. L. Rayz, and R. M. D'Souza. Merging computational fluid dynamics and 4D Flow MRI using proper orthogonal decomposition and ridge regression. *J Biomech*. 58:162–173, 2017. https://doi.org/10.1016/j.jbiomech.2017.05.004.
15. Perez-Raya, I., M. F. Fathi, A. Baghaie, R. H. Sacho, K. M. Koch, and R. M. D'Souza. Towards multi-modal data fusion for super-resolution and denoising of 4D-Flow MRI. *Int J Numer Method Biomed Eng*.36(9):e3381, 2020. https://doi.org/10.1002/cnm.3381.
16. Funke, S. W., M. Nordaas, O. Evju, M. S. Alnaes, and K. A. Mardal. Variational data assimilation for transient blood flow simulations: Cerebral aneurysms as an illustrative example. *Int J Numer Method Biomed Eng*.35(1):e3152, 2019. https://doi.org/10.1002/cnm.3152.
17. Rispoli, V. C., J. F. Nielsen, K. S. Nayak, and J. L. Carvalho. Computational fluid dynamics simulations of blood flow regularized by 3D phase contrast MRI. *Biomed Eng Online*. 14:110, 2015. https://doi.org/10.1186/s12938-015-0104-7.
18. Toger, J., M. J. Zahr, N. Aristokleous, K. Markenroth-Bloch, M. Carlsson, and P. O. Persson. Blood flow imaging by optimal matching of computational fluid dynamics to 4D-flow data. *Magn Reson Med*. 84(4):2231–2245, 2020. https://doi.org/10.1002/mrm.28269.
19. Zhang, J., M. Brindise, S. Rothenberger, M. Markl, V. Rayz, and P. Vlachos. A multi-modality approach for enhancing 4D flow magnetic resonance imaging via sparse representation. *Journal of The Royal Society Interface*. 19:4, 2022. https://doi.org/10.1098/rsif.2021.0751.
20. Fathi, M. F., et al. Super-resolution and denoising of 4D-Flow MRI using physics-Informed deep neural nets. *Computer Methods and Programs in Biomedicine*.197:105729, 2020. https://doi.org/10.1016/j.cmpb.2020.105729.
21. Ferdian, E., et al. 4DFlowNet: Super-Resolution 4D Flow MRI Using Deep Learning and Computational Fluid Dynamics. *Frontiers in Physics*. 8:9, 2020. https://doi.org/10.3389/fphy.2020.00138.
22. Gao, H., L. Sun, and J.-X. Wang. Super-resolution and denoising of fluid flow using physics-informed convolutional neural networks without high-resolution labels. *Physics of Fluids*.33(7):073603, 2021. https://doi.org/10.1063/5.0054312.
23. Rutkowski, D. R., A. Roldan-Alzate, and K. M. Johnson. Enhancement of cerebrovascular 4D flow MRI velocity fields using machine learning and computational fluid dynamics simulation data. *Sci Rep*. 11(1):10240, 2021. https://doi.org/10.1038/s41598-021-89636-z.

24. Shit, S., J. Zimmermann, I. Ezhov, J. Paetzold, A. Sanches, C. Pirkl, and B. Menze. SRflow: Deep learning based super-resolution of 4D-flow MRI data. *Frontiers in Artificial Intelligence*. 2022. https://doi.org/10.3389/frai.2022.928181.
25. Y. Chen, A. G. Christodoulou, Z. Zhou, F. Shi, Y. Xie, and D. Li, "MRI Super-Resolution with GAN and 3D Multi-Level DenseNet: Smaller, Faster, and Better," 2020, https://doi.org/10.48550/arXiv.2003.01217.
26. Y. L. Ze Liu, Yue Cao, Han Hu, Yixuan Wei, Zheng Zhang, Stephen Lin, Baining Guo, "Swin Transformer: Hierarchical Vision Transformer using Shifted Windows," 2021, https://doi.org/10.48550/arXiv.2103.14030.
27. A. Daw, Karpatne, A, Watkins, W, Read, J, Kumar, V, "Physics-guided Neural Networks (PGNN): An Application in Lake Temperature Modeling," 2017, https://doi.org/10.48550/arXiv.1710.11431.
28. Yushkevich, P. A., et al. User-guided 3D active contour segmentation of anatomical structures: Significantly improved efficiency and reliability. *NeuroImage*. 31(3):1116–1128, 2006. https://doi.org/10.1016/j.neuroimage.2006.01.015.
29. *HyperMesh*. (2017). Altair Engineering, Inc., Troy, MI, USA.
30. Daouk, J., et al. Relationship between cerebrospinal fluid flow, ventricles morphology, and DTI properties in internal capsules: differences between Alzheimer's disease and normal-pressure hydrocephalus. *Acta Radiologica*. 55(8):992–999, 2014. https://doi.org/10.1177/0284185113508112.
31. *Ansys 19.2*. (2018). Ansys®, Canonsburg, PA, USA.
32. van Leer, B. Towards the ultimate conservative difference scheme. V. A second-order sequel to Godunov's method. *Journal of Computational Physics*. 32(1):101–136, 1979. https://doi.org/10.1016/0021-9991(79)90145-1.
33. Rothenberger, S. M., et al. Modeling Bias Error in 4D Flow MRI Velocity Measurements. *IEEE Transactions on Medical Imaging*. 41(7):1802–1812, 2022. https://doi.org/10.1109/tmi.2022.3149421.
34. Zhang, J., et al. 4D Flow MRI Pressure Estimation Using Velocity Measurement-Error-Based Weighted Least-Squares. *IEEE Trans Med Imaging*. 39(5):1668–1680, 2020. https://doi.org/10.1109/TMI.2019.2954697.
35. Y. C. Fung, "Blood Flow in Arteries," in *Biomechanics: Circulation*, Y. C. Fung Ed. New York, NY: Springer, 1997, pp. 108-205.
36. Andersen, A. H., and J. E. Kirsch. Analysis of noise in phase contrast MR imaging. *Medical Physics*. 23(6):857–869, 1996. https://doi.org/10.1118/1.597729.
37. J. Zhang *et al.*, "Divergence-Free Constrained Phase Unwrapping and Denoising for 4D Flow MRI Using Weighted Least-Squares," *IEEE Trans Med Imaging,* vol. PP, Jun 4 2021, https://doi.org/10.1109/TMI.2021.3086331.
38. Cárdenas-Blanco, A., C. Tejos, P. Irarrazaval, and I. Cameron. Noise in magnitude magnetic resonance images. *Concepts in Magnetic Resonance Part A*. 32A(6):409–416, 2008. https://doi.org/10.1002/cmr.a.20124.
39. D. G. Nishimura, *Principles of Magnetic Resonance Imaging*. 2016.
40. G. Huang, Z. Liu, L. van der Maaten, and K. Weinberger, "Densely Connected Convolutional Networks," *CVPR* 2017.
41. I. Misra, A. Shrivastava, A. Gupta, and M. Hebert, "Cross-stitch Networks for Multi-task Learning," 2016, https://doi.org/10.48550/arXiv.1604.03539.
42. A. Paszke, et al, "PyTorch: An Imperative Style, High-Performance Deep Learning Library," *Advances in Neural Information Processing Systems.,* pp. 8024-8035, 2019. Available: http://papers.neurips.cc/paper/9015-pytorch-an-imperative-style-high-performance-deep-learning-library.pdf.
43. R. Liaw, Liang, E, Nishihara, R, Moritz, P, Gonzalez, J, and Stoica, I, "Tune: A Research Platform for Distributed Model Selection and Training," 2018. Available: https://arxiv.org/pdf/1807.05118.pdf.
44. L. Li, Jamieson, K., Rostamizadeh, A., Gonina, E., Ben-Tzur, J., Hardt, M., Recht, B., Talwalkar, A., "A System for Massively Parallel Hyperparameter Tuning," presented at the MLSys Conference, Austin, TX, USA, 2020.
45. Schnell, S., et al. Accelerated dual-venc 4D flow MRI for neurovascular applications. *Journal of Magnetic Resonance Imaging*. 46(1):102–114, 2017. https://doi.org/10.1002/jmri.25595.
46. *Geomagic Design X*. (2019). 3D Systems, Circle Rock Hill, SC, USA.
47. J. P. Ahrens, B. Geveci, and C. C. Law, "ParaView: An End-User Tool for Large-Data Visualization," in *The Visualization Handbook*, 2005.
48. Gholampour, S., and N. Fatouraee. Boundary conditions investigation to improve computer simulation of cerebrospinal fluid dynamics in hydrocephalus patients. *Communications Biology*. 2021. https://doi.org/10.1038/s42003-021-01920-w.
49. Stadlbauer, A., E. Salomonowitz, W. van der Riet, M. Buchfelder, and O. Ganslandt. "Insight into the patterns of cerebrospinal fluid flow in the human ventricular system using MR velocity mapping," (in eng). *Neuroimage*. 51(1):42–52, 2010. https://doi.org/10.1016/j.neuroimage.2010.01.110.
50. Rivera-Rivera, L. A., T. Vikner, L. Eisenmenger, S. C. Johnson, and K. M. Johnson. Four-dimensional flow MRI for quantitative assessment of cerebrospinal fluid dynamics: Status and opportunities. *NMR in Biomedicine*. 2024. https://doi.org/10.1002/nbm.5082.
51. Rivera-Rivera, L. A., et al. 4D flow MRI for intracranial hemodynamics assessment in Alzheimer's disease. *Journal of Cerebral Blood Flow & Metabolism*. 36(10):1718–1730, 2016. https://doi.org/10.1177/0271678x15617171.
52. Nishimura, D., J. Jackson, and J. Pauly. On the nature and reduction of the displacement artifact in flow images. *Magn Reson Med*. 22(2):481–492, 1991. https://doi.org/10.1002/mrm.1910220255.
53. Fultz, N. E., et al. Coupled electrophysiological, hemodynamic, and cerebrospinal fluid oscillations in human sleep. *Science*. 366(6465):628–631, 2019. https://doi.org/10.1126/science.aax5440.
54. B. Jung and M. Markl, "Phase-Contrast MRI and Flow Quantification," in *Magnetic Resonance Angiography*: Springer New York, 2012, pp. 51-64.
55. Peeters, J. M., C. Bos, and C. J. G. Bakker. Analysis and correction of gradient nonlinearity and B0 inhomogeneity related scaling errors in two-dimensional phase contrast flow measurements. *Magnetic Resonance in Medicine*. 53(1):126–133, 2005. https://doi.org/10.1002/mrm.20309.
56. Markl, M., et al. Generalized reconstruction of phase contrast MRI: analysis and correction of the effect of gradient field distortions. *Magn Reson Med*. 50(4):791–801, 2003. https://doi.org/10.1002/mrm.10582.
57. Bernstein, M. A., et al. "Concomitant gradient terms in phase contrast MR: analysis and correction," (in eng). *Magn Reson Med*. 39(2):300–308, 1998. https://doi.org/10.1002/mrm.1910390218.
58. Detmer, F. J., et al. Development and internal validation of an aneurysm rupture probability model based on patient characteristics and aneurysm location, morphology, and hemodynamics. *Int J Comput Assist Radiol Surg*. 13(11):1767–1779, 2018. https://doi.org/10.1007/s11548-018-1837-0.
59. Xiang, J., et al. Hemodynamic-morphologic discriminants for intracranial aneurysm rupture. *Stroke*. 42(1):144–152, 2011. https://doi.org/10.1161/STROKEAHA.110.592923.
60. Xiang, J., J. Yu, K. V. Snyder, E. I. Levy, A. H. Siddiqui, and H. Meng. Hemodynamic-morphological discriminant models for intracranial aneurysm rupture remain stable with increasing

sample size. *J Neurointerv Surg*. 8(1):104–110, 2016. https://doi.org/10.1136/neurintsurg-2014-011477.